# Modelling Local Bubble analogs: synthetic dust polarization maps

E. Maconi,[1,2,3]⋆ J. D. Soler,[4]⋆ S. Reissl,[1] P. Girichidis [ID],[1] R. S. Klessen [ID],[1,5] P. Hennebelle,[6]
S. Molinari [ID],[4] L. Testi,[7] R. J. Smith [ID],[8] M. C. Sormani [ID],[1] J. W. Teh [ID][1] and A. Traficante [ID][4]

[1]*Zentrum für Astronomie, Institut für Theoretische Astrophysik, Universität Heidelberg, Albert-Ueberle-Straße 2, D-69120 Heidelberg, Germany*
[2]*Physics Department, Università degli Studi di Milano-Bicocca, piazza della Scienza 3, I-20126 Milan, Italy*
[3]*Institut für Astrophysik, Universität Wien, Türkenschanzstrasse 17, A-1180 Wien, Austria*
[4]*Istituto di Astrofisica e Planetologia Spaziale, INAF, Via Fosso del Cavaliere 100, I-00133 Roma, Italy*
[5]*Interdisziplinäres Zentrum für Wissenschaftliches Rechnen, Universität Heidelberg, Im Neuenheimer Feld 205, D-69120 Heidelberg, Germany*
[6]*AIM, CEA, CNRS, Université Paris-Saclay, Université Paris Diderot, Sorbonne Paris Cité, F-91191 Gif-sur-Yvette, France*
[7]*Dipartimento di Fisica e Astronomia 'Augusto Righi', Viale Berti Pichat 6/2, I-40126 Bologna, Italy*
[8]*Jodrell Bank Centre for Astrophysics, Department of Physics and Astronomy, University of Manchester, Oxford Road, Manchester M13 9PL, UK*

## ABSTRACT

We present a study of synthetic observations of polarized dust emission at 353 GHz as seen by an observer within a cavity in the interstellar medium (ISM). The cavity is selected from a magnetohydrodynamic simulation of the local ISM with time-dependent chemistry, star formation, and stellar feedback in form of supernova explosions with physical properties comparable to the Local Bubble ones. We find that the local density enhancement together with the coherent magnetic field in the cavity walls makes the selected candidate a translucent polarization filter to the emission coming from beyond its domains. This underlines the importance of studying the Local Bubble in further detail. The magnetic field lines inferred from synthetic dust polarization data are qualitatively in agreement with the all-sky maps of polarized emission at 353 GHz from the *Planck* satellite in the latitudes interval $15° \lesssim |b| \lesssim 65°$. As our numerical simulation allows us to track the galactic mid-plane only out to distances of 250 pc, we exclude the region $|b| \lesssim 15°$ from our analysis. At large galactic latitudes, our model exhibits a high degree of small-scale structures. On the contrary, the observed polarization pattern around the Galactic Poles is relatively coherent and regular, and we argue that the global toroidal magnetic field of the Milky Way is important for explaining the data at $|b| \gtrsim 65°$. We show that from our synthetic polarization maps, it is difficult to distinguish between an open and a closed galactic cap using the inferred magnetic field morphology alone.

**Key words:** polarization – ISM: bubbles – ISM: general – ISM: magnetic fields.

## 1 INTRODUCTION

Astronomical observations of interstellar reddening and soft-diffuse X-rays indicate that the Sun lies within a cavity of low-density, high-temperature, and warm plasma surrounded by a shell of cold, neutral gas and dust (see e.g. Sanders et al. 1977; Lucke 1978; Cox & Reynolds 1987; Snowden et al. 2015; Linsky & Redfield 2021; Zucker et al. 2022). The edges of this cavity, commonly called the 'Local Bubble', are producing a portion of the signal in the observations of dust-polarized thermal emission used in the study of the Galactic magnetic field and the foreground to cosmic microwave background (CMB) radiation (Planck Collaboration XLII 2016b; Planck Collaboration IX 2020). Therefore, understanding the polarization signal produced by the Local Bubble is of crucial importance for Galactic astronomy and cosmology.

Starlight polarization at optical-to-infrared wavelengths and dust-polarized emission most likely arise from asymmetric dust grains that are aligned perpendicular to the magnetic field lines (see Andersson,

Lazarian & Vaillancourt 2015, for a review). For a long time, extended polarization maps were restricted to observations of the stellar polarization data available for a discrete set of lines of sight (LOSs; Heiles 2000). The convergence of the starlight polarization orientations towards the presumed tangent points of the local spiral arm motivated the modelling of the polarized signal as the result of the curvature of the Galactic magnetic field (Heiles 1996). In that model, the local magnetic field closely follows the curvature of the spiral arm, as observed in other galaxies (Beck 2013; Borlaff et al. 2021), and the convergence of the field lines is an effect of our perspective as observers within the arm.

The European Space Agency's *Planck* satellite produced the first all-sky map of the polarized emission from dust at sub-millimetre wavelengths (Planck Collaboration I 2016a). The *Planck* map of the polarized emission at 353 GHz revealed a regular pattern of magnetic field orientations toward the Galactic caps (Planck Collaboration XLIV 2016c). Inspired by the regular pattern produced by the expansion of a super-bubble in a uniform magnetic field, researchers have modelled the *Planck* observations as the result of a magnetic field frozen into the walls of an inclined spheroidal bubble (Ferriere, Mac Low & Zweibel 1991; Alves et al. 2018; Pelgrims et al. 2020).

⋆ E-mail: e.maconi1@campus.unimib.it (EM); juandiegosolerp@gmail.com (JDS)

**Table 1.** Key properties of the Local Bubble.

| Quantity | | Value | Reference |
|---|---|---|---|
| Shell total mass | $M_{\text{shell}}$ | $1.4 \times 10^6 \, M_\odot$ | Zucker et al. (2022) |
| Shell expansion velocity | $v_{\text{shell}}$ | $6.7 \, \text{km s}^{-1}$ | Zucker et al. (2022) |
| Thermal pressure | $P/k_{\text{B}}$ | $10\,700 \, \text{cm}^{-3} \, \text{K}$ | Snowden et al. (2014) |
| Mean field strength | $<|B|>$ | 0.5 to 2 $\mu$G | Xu & Han (2019) |

In this paper, we present a study of the polarization imprint produced by a Local Bubble-like cavity identified in magnetohydrodynamic (MHD) simulations of a multiphase stratified medium with overall properties selected to match the Milky Way at the solar radius. The numerical simulations are part of the SImulating the Life-Cycle of molecular Clouds (SILCC) project (Walch et al. 2015; Girichidis et al. 2016). Once the candidate cavity has been selected, the radiative transfer (RT) code POLARIS (Reissl, Wolf & Brauer 2016; Reissl et al. 2019) is used to produce synthetic dust polarization emission maps at 353 GHz for an observer placed inside the bubble analogue. Thanks to the RT simulations, the 3D information remains accessible along each LOS and the origin of the polarized signal can be explored.

This paper is organized as follows. In Section 2, the known properties of the Local Bubble are reviewed. Section 3 presents the MHD numerical simulations, the bubble selection process, and the method used to identify the cavity walls. Section 4 describes the postprocessing set-up used to produce the synthetic observations. The results are discussed in Section 5 and the conclusions are presented in Section 6.

## 2 PROPERTIES OF THE LOCAL BUBBLE

The Local Bubble is thought to be the product of star formation and supernova (SN) explosions that occurred over the past 10–15 Myr, as recently reconstructed by Zucker et al. (2022). The modelling of the cavity expansion and the tracing back of the solar orbit indicates that the Sun entered the Local Bubble approximately 5 Myr ago. Additional SN explosions have been linked to anomalous concentrations of the radionuclide $^{60}$Fe in deep-sea layers dating from about 2.2 Myr ago (Breitschwerdt et al. 2016; Schulreich et al. 2018). The mass of gas swept away by the SN explosions, and which now forms the shell, has been estimated in $M_{\text{shell}} = (1.4 \pm 0.6) \times 10^6 \, M_\odot$ and this shell is still expanding with a velocity of $v_{\text{shell}} = (6.7 \pm 0.4) \, \text{km s}^{-1}$ (Zucker et al. 2022).

The high-temperature plasma enclosed by the Local Bubble shell was identified as the source of the unexpectedly intense diffuse flux of 0.25 keV X-rays observed over the whole sky by the *ROSAT* satellite (Snowden et al. 1997; Galeazzi et al. 2014; Puspitarini et al. 2014; Snowden et al. 2015). The nature of the inner environment of the Local Bubble, whether it consists of a low-density million-degree plasma ($10^6$ K) heated by SN shocks or a combination of hot and warm (10 000–20 000 K) components, is still a subject of ongoing debate (see e.g. Linsky & Redfield 2021).

The Local Bubble was identified as the origin of the high-latitude radio emission measured by the ARCADE 2 balloon-borne telescope and other instruments at frequencies below about 3 GHz (Sun et al. 2008; Krause & Hardcastle 2021). More recently, the dusty boundary of the Local Bubble was mapped using the extinction in the emission from stars with known distances (Lallement et al. 2014; Zucker et al. 2022).

Table 1 summarizes the main Local Bubble properties, which are derived as follows. The thermal pressure of the plasma in the Local

Bubble $P/k_{\text{B}} = 10\,700 \, \text{cm}^{-3} \, \text{K}$ is derived from the combination of the magnetic field measurement outside of the heliosphere by the Voyager 1 spacecraft and the soft X-rays observations from sounding rockets and the *ROSAT* satellite (Snowden et al. 2014). The X-ray emission leads to a thermal electron density $n_{e,X} = (4.68 \pm 0.47) \times 10^{-3} \, \text{cm}^{-3}$, which is typical for superbubbles, including X-ray bright ones, as shown in 3D numerical simulations (see e.g. Krause et al. 2013a, b).

Using the Faraday rotation measure (RM) of 494 pulsars within 3 kpc from the Sun, Xu & Han (2019) estimated that the Local Bubble edge is located at between 80 and 140 pc from the Sun. These observations indicate that the Local Bubble's mean magnetic field strength is between 0.5 and 2.0 $\mu$G. For eight pulsars close to the edge of the Local Bubble, Xu & Han (2019) report a mean dispersion measure (DM) of 42 $\text{cm}^{-3}$ pc with a standard deviation of 20 $\text{cm}^{-3}$ pc, which corresponds to a column of free, thermal electrons $N_e = (1.3 \pm 0.6) \times 10^{20} \, \text{cm}^{-2}$.

The column density of free electrons and the RM are most likely produced by the bubble wall, in the ionized mixing layer between the bubble interior and the cold shell (Xu & Han 2019). Warm clouds within the Local Bubble have characteristic sizes of several parsecs and electron densities of the order of $n_{e,WC} = 10^{-1} \, \text{cm}^{-3}$ (see e.g. Gry & Jenkins 2017; Linsky, Redfield & Tilipman 2019). Assuming a total warm cloud path length of 10 pc, the corresponding free electron column is $N_{e,wc} = 3 \times 10^{18} \, \text{cm}^{-2}$. Hence, neither the hot X-ray plasma nor the warm clouds and filaments contribute significantly to the pulsar DMs.

## 3 SIMULATED LOCAL BUBBLE

### 3.1 Simulation and selection of the bubble

We identify a Local Bubble candidate in the set of numerical simulations presented in Girichidis et al. (2018) and Girichidis (2021), which are part of the SILCC project (Walch et al. 2015; Girichidis et al. 2016). These simulations consider a multiphase medium in a domain of a $500 \times 500 \times 500 \, \text{pc}^3$ with conditions close to the local neighbourhood in terms of the total gas surface density ($\langle \Sigma_{\text{gas}} \rangle = 10 \, M_\odot \, \text{pc}^{-2}$), the velocity dispersion ($\langle v_{\text{gas}} \rangle \sim 10 \, \text{km s}^{-1}$), the average magnetization ($B \sim 0.1 - 10 \, \mu$G) as well as the chemical composition and the local rate of SN explosions (see Girichidis et al. 2018). The simulations run with an adaptive mesh refinement with the highest resolution set to 0.98 pc.

The initial gas distribution is stratified following a Gaussian profile with a scale height of 60 pc, aiming to reproduce the conditions in a portion of the Galactic plane approximately at the solar radius. The gas is initially at rest and in pressure equilibrium. The initial magnetic field is set along the $x$ direction and has a central intensity of $B(z = 0) = 3 \, \mu$G, that scales in the vertical direction as $B(z) = B(z = 0)(\rho(z)/\rho(z = 0))^{1/2}$.

The simulations include SN feedback, which stirs the medium and creates a three-phase medium comparable to the observed local interstellar medium (ISM). The individual and clustered SN

explosions create dense filaments and clouds of cold gas, mainly in the regions in which shells collide, and hot voids, primarily close to the local explosion sites of clustered SN.

We collect a series of snapshots from the simulations and proceed by selecting a set of bubbles by eye in each time-step. For each bubble, we compute the average density, the total mass in ionized gas, and the mass- and volume-weighted magnetic field and temperature in order to identify the cavity whose properties best match the Local Bubble. Our candidate bubble results from the explosion of 17 clustered SN explosions, in agreement with the 14–20 SN events that appear to be responsible for the Local Bubble (Fuchs et al. 2006). In our simulation, the gas mass swept away by the SN explosions is $M_{shell} \sim 2 \times 10^5\,M_\odot$, an order of magnitude lower compared to Zucker et al. (2022). However, we would like to emphasize that the total energy driving the expansion of the cavity is more important than the shell mass. For one thing, the measured mass of the shell around the bubble depends on the integration length and the structure of the surrounding medium. In particular, if the vicinity of the bubble is highly structured a significant fraction of the shell mass is located in small concentrated clouds. In fact, in the Paper of Zucker et al. (2022) the estimate of the shell mass around the Local Bubble includes the nearby clouds such as Taurus and Ophiuchus (private communication), which we do not have in our simulation. Consequently, the amount of locally concentrated mass only occupies a very small solid angle and the analysis of the full sky around the Local Bubble is only marginally affected by such high density nearby clouds. Moreover, we aim to select a cavity that best fits the properties of the Local Bubble, but we are aware of the impossibility of finding a perfect candidate. For more information on the simulations setup and on the selection of the candidate cavity, we refer the reader to Appendix A and to Girichidis (2021).

Fig. 1 shows the gas density, the gas temperature, and the total magnetic field strength for the candidate bubble in cuts through the centre. The bottom panel of Fig. 1 also reports the dust temperature computed by POLARIS, as further discussed in Section 4. The figure illustrates that our cavity is not isolated but surrounded by other expanding bubbles, which influence each other as they expand. This picture is in agreement with the observed structure of the local ISM, where the Local Bubble coexists with other SN-blown cavities (see e.g. Soler, Bracco & Pon 2018; Bracco et al. 2020; Bialy et al. 2021; Zucker et al. 2022). Moreover, since the selected cavity has an open and a closed cap, we can study the differences in polarization properties and column density between the two configurations; this has observational value because evidence suggests that the local interstellar cavity could be open in the Galactic halo, forming the so-called Local Chimney (Cox & Smith 1974; Welsh et al. 1999; Lallement et al. 2003; Zucker et al. 2022).

## 3.2 Defining the walls of the simulated bubble

Once we identify a possible Local Bubble candidate in the simulations, we determine the inner surface of the cavity using the column density maps provided by POLARIS. POLARIS allows an angular sampling of the celestial sphere according to a HEALPIX pixelization (Górski et al. 2005). We measure the emerging polarization signal and the column density values on 70 concentric spheres centred on the cavity and with an increasing radius step of 5 pc. Each sphere is divided into 786 432 pixels, corresponding to the HEALPIX parameter $N_{side} = 256$ and to an angular resolution of $13\rlap{.}'7$.

For each LOS, we construct a radial profile of the column density $N_H(r)$, with $r$ being the distance from the cavity centre i.e. the observer. We define the radius of the Local Bubble inner surface ($r_{in}$) as the distance from the cavity centre, starting from the observer

and going outward, at the location where $N_H$ has its first relative increase greater than 0.9 per cent. We choose this value empirically after several attempts. We avoid the selection of isolated dense structures within the cavity by setting a threshold on temperature and magnetic field strength. If the temperature and magnetic field at the selected point are greater than $10^{4.5}$ K and less than $10^{-1.2}\,\mu G$, it is not registered as part of the cavity wall.

The outer surface of the Local Bubble candidate is established following the procedure defined in Pelgrims et al. (2020), where the geometry of the Local Bubble shell is determined using the relative values of the observed dust density. In their work, they draw LOSs starting from the Sun and going outward, with a radial sampling step of 2.5 pc, and, for each LOS, they compute the differential extinction $A'_V(r)$. The inner surface of the Local Bubble, $r_{inner}$, is then defined as the distance to the first point where the curve has a change from convex to concave. Similarly, the outer surface of the cavity is defined as the point, after $r_{inner}$, where $A'_V(r)$ changes from concave to convex.

We use the Pelgrims et al. (2020) method to determine the outer shell of our Local Bubble candidate, giving as input the inner surface radius previously computed. We smooth the $N_H$ HEALPIX maps with a Gaussian symmetric beam ($\sigma = 0.015$ rad) and we compute, for each LOS, the differential of the column density $\Delta N_H(r)$ and its first and second derivatives with respect to the radius. The outer surface radius ($r_{out}$) is set to be the distance where the curves have their first inflection point beyond the inner wall. Due to the complexity of gas distribution, this method to find the Local Bubble walls may fail in some directions but we can confirm this is only the case for a small percentage of LOSs. We show the differential column density curves for eight LOSs selected in the $x$–$y$ plane in Fig. 2. We calculate the cavity thickness as the mean value of $r_{out} - r_{in}$, which for our cavity results in ∼14 pc. The HEALPIX spherical-coordinate information, which describes the computed distance to the Local Bubble walls along every LOS, is later used in this paper to select the part of the bubble enclosed by the outer wall and to study its influence on the polarization of light.

In Fig. 3, the gas density is depicted together with the inner and outer surfaces; in Fig. 4, a full-sky map of the distance to the inner surface of the cavity is presented. For the orientation convention of the full-sky map, we refer the reader to Section 4.3.

## 4 RADIATIVE TRANSFER SIMULATION

All the results presented here are obtained with the same post-processing scheme. To compute the dust temperature, the dust grain alignment efficiency and to produce synthetic polarization maps with the relative Stokes' parameters, we make use of the RT code POLARIS. We refer the reader to Appendix B and to Reissl et al. (2016) for a more in-depth view of the POLARIS RT scheme.

### 4.1 Post-processing set-up

As a first step, we calculate with POLARIS the dust temperature and the grain alignment efficiency, having given as input the gas density, the gas temperature, the magnetic fields, the dust model, and the sources of emitting photons. Our dust component is based on a canonical model of the ISM, with a constant dust-to-gas ratio $m_{dust}/m_{gas} = 0.01$ in each grid cell and it consists of a mixture of astronomical silicate (37.5 per cent) and graphite (62.5 per cent) materials. To trace dust polarization, we consider non-spherical dust grains with a size range from $a_{min} = 5$ nm to $a_{max} = 200$ nm and a size distribution following
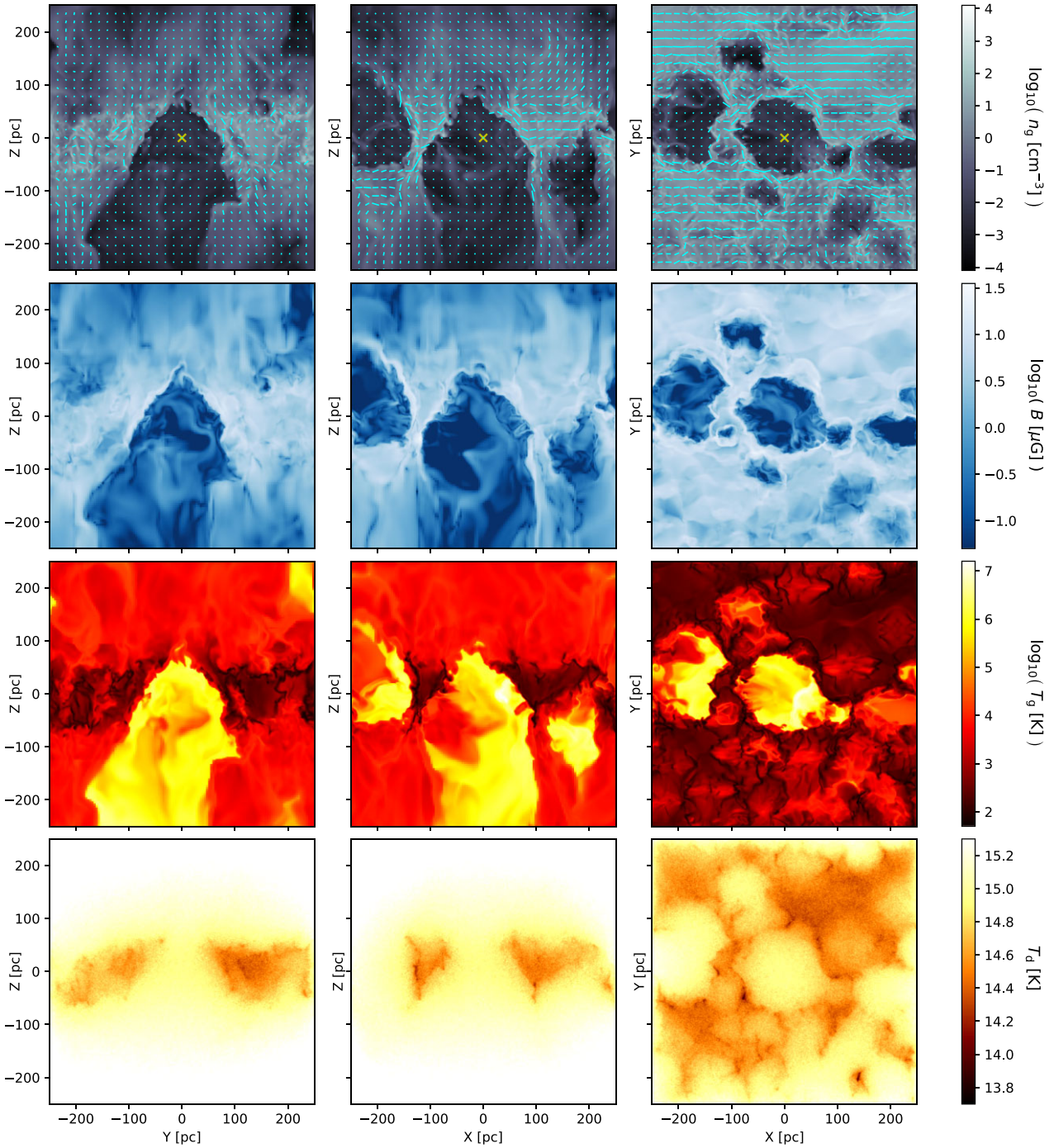
**Figure 1.** From top to bottom: gas number density ($n_g$), total magnetic field strength ($B$), gas temperature ($T_g$), and dust temperature ($T_d$) in 1-pc-thick cuts of the simulation domain centred on the Local Bubble candidate. The top panel shows the orientation of the magnetic field, in cyan pseudo-vectors normalized to $|\mathbf{B}_{\mathrm{max}}|$; the position of the observer used in the synthetic observations is shown as a yellow cross.

a power law of $N_d(a) \propto a^{-3.5}$, where $a$ is the effective radius of a non-spherical dust grain equivalent to the volume of a sphere of the same mass (Dohnanyi 1969; Mathis, Rumpl & Nordsieck 1977).

As a source of emitting photons, we assume a Mathis' interstellar radiation field (ISRF; Mathis, Mezger & Panagia 1983; Camps et al. 2015) which takes into account the typical stellar emission and the dust thermal radiation in the Milky Way as well as the contribution

of the CMB. For the ISRF, we assume a strength factor $G_0 = 1.6$ with $2 \times 10^8$ photon packages, which is a good compromise between run-time and noise.
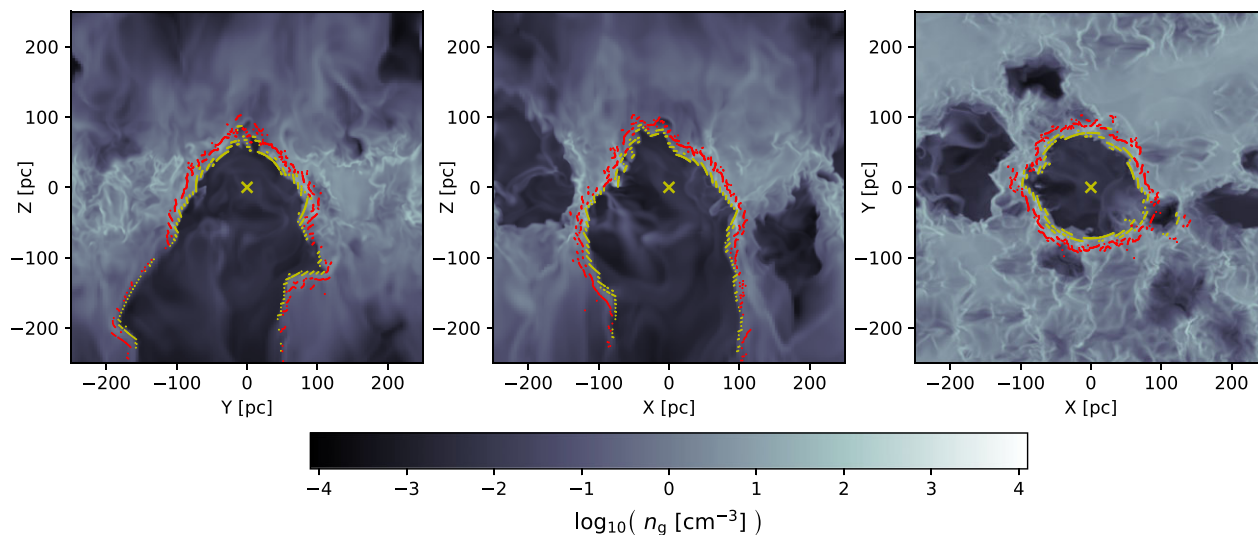
As a second step, we perform a ray-tracing simulation at a frequency of 353 GHz for an observer placed at the very centre of the cavity. We use the same setup adopted to find the bubble walls: 70 concentric spheres spaced by 5 pc apart are used to sample the celestial sphere according to the HEALPIX pixelization
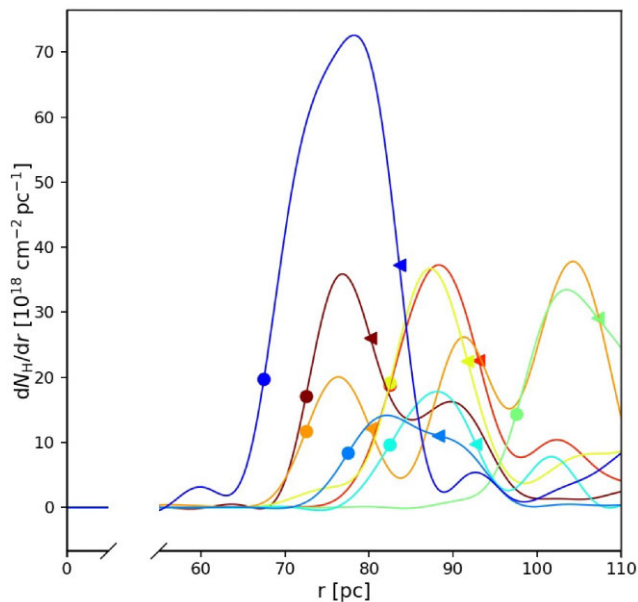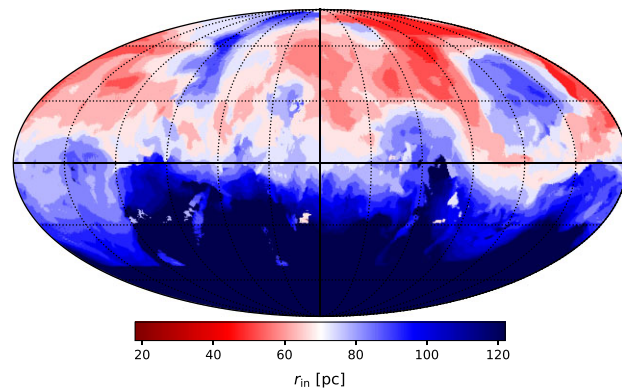
**Figure 2.** Radial profiles of the differential column density $dN_H(r)/dr$ are shown for eight LOSs in the *x–y* plane equally spaced by 45°. The inner and outer boundaries of the selected cavity, as computed in Section 3.2, are indicated on each curve with a filled circle and triangle, respectively.



**Figure 4.** Mollweide projection of the distance to the inner surface of the Local Bubble candidate, $r_{in}$, as identified using the method described in Section 3.2.
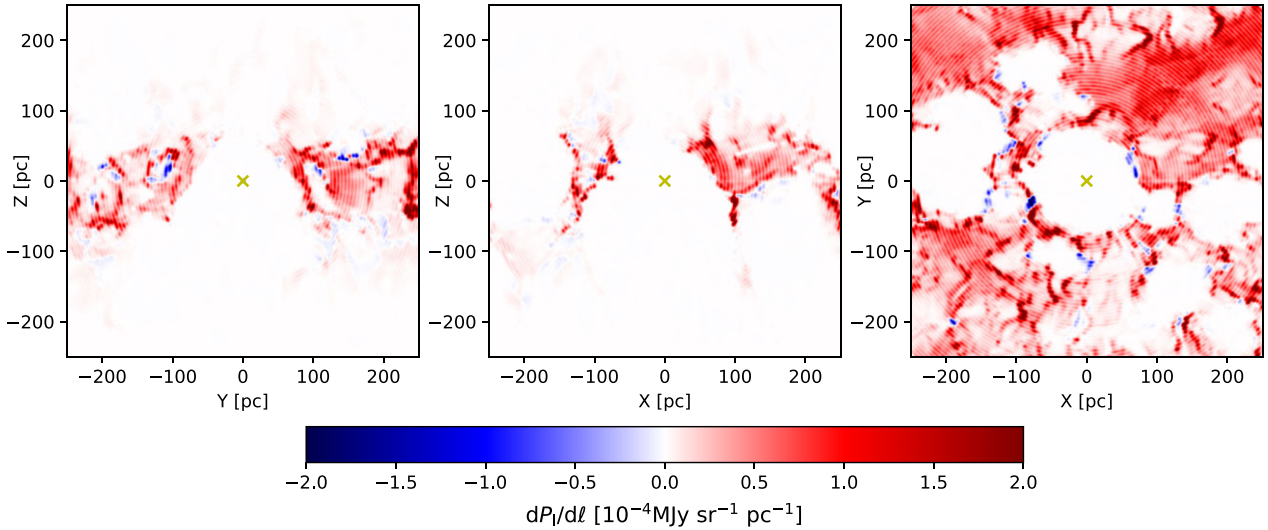
**Table 2.** Synthetic observations overview.

| Simulation name | Density field | Magnetic field |
|---|---|---|
| S0 | Original | Original |
| S0justLB | Enclosed by the outer edge | Original |
| S0uniB | Original | $\mathbf{B} = (1.8 \ \mu G) \ \hat{x}$ |

We emphasize that at 353 GHz the dust polarization is perpendicular to the magnetic field and $\psi$ needs to be rotated by 90° to infer the magnetic field orientation.

### 4.2 Line-of-sight analysis technique

The transport of radiation is a 3D problem but, unfortunately, in any astronomical observation of radiation emitted by the dust one of the spatial dimensions is lost. The advantage of synthetic observations made with an RT post-processing technique is that the 3D information remains accessible along each LOS and, as a consequence, the

(Górski et al. 2005, $N_{side} = 256$). POLARIS returns, for each LOS, the column density, the optical depth, and the relative Stokes' vector $\mathbf{S} = (I, Q, U, V)^T$, where $I$ is the total intensity, $Q$ and $U$ represent the linear polarization, and $V$ is the circular polarization. For each LOS, we can therefore determine the linear polarized intensity $P_l$, the degree of linear polarization $p_l$, and the polarization angle $\psi$,

$$P_l = \sqrt{Q^2 + U^2}, \quad p_l = \frac{P}{I}, \quad \psi = \frac{1}{2} \tan^{-1} \left( \frac{U}{Q} \right). \quad (1)$$



**Figure 3.** Gas number density at the simulation mid-planes. The yellow and red line segments mark the position of the inner and outer surfaces of the Local Bubble candidate, respectively. The yellow cross represents the observer's position.

**Figure 5.** Same as Fig. 1, but for the first derivative of the linearly polarized flux at 353 GHz along the LOS, $dP_{353}/dr = (P_{353}(r + dr) - P_{353}(r))/dr$, calculated in the synthetic observation produced using POLARIS. The red (blue) colours correspond to increases (decreases) in $P_{353}$ along each LOS towards an observer at the position at the centre marked by a yellow cross, respectively. The concentric ring regular pattern visible in the images is due to the finite number of detectors used to sample the rays of light.

origin of the polarized signal can be explored in hindsight. The procedure is similar to that introduced in Reissl et al. (2020b). To track the polarization signal, we defined a series of concentric HEALPIX detectors; in such a way, we can evaluate the first derivative of the signal along each path element $dr$ of the LOS as

$$\Delta x_i(r) = \frac{x_i(r + dr) - x_i(dr)}{dr}, \quad (2)$$

where $x$ can represent e.g. the intensity or the polarized intensity, and the index $i$ stands for a distinct position along a certain LOS, i.e. a pixel of the HEALPIX map. Using the just defined quantity and computing its cumulative, we can evaluate the accumulated value $x$ up to a given distance

$$x_i(r) = \int_0^r \Delta x_i(r') \, dr', \quad (3)$$

where $r$ is the distance from the observer. We study the origin of the polarization signal along all LOSs and the contribution of the local environment, i.e. the cavity walls, to the properties of the received light.

### 4.3 Mollweide and orthographic projections orientation

We present full-sky maps and orthographic views of the data whose orientation is decided and defined as follows.

The orientation of the maps is constrained by the initial magnetic field orientation of our simulation (parallel to the $x$-axis; see Section 3.1) and by the one observed in our location in the Milky Way. We therefore set the centre of the full-sky maps, $(l, b) = (0°, 0°)$, to coincide with the LOS that propagates from the observer toward the $-y$ direction in the $x - y$ plane; here $l$ and $b$ are the longitude and the latitude, respectively. The $-y$ direction can be considered as the LOS toward the hypothetical galactic centre of our simulation. Moving from $(l, b) = (0°, 0°)$ to the left (positive increase in longitude) is equivalent to moving in a clockwise direction in the $x$–$y$ plane from the starting LOS; moving from centre to the right is instead equivalent to moving in a counterclockwise direction.

In the orthographic projections, the left-hand and right-hand panels touch at $l = -90°$; $l = 0°$ coincide with the lower point of the circle.

## 5 RESULTS AND DISCUSSION

We expect the walls of the cavity to have an impact on the polarization observations performed inside it, since dust will act both as a polarizing filter and as a source of polarized light alike. Indeed, compared to the larger scale environment, the bubble edges have a greater dust density, as a natural result of the cavity expansion; moreover, they are crossed by magnetic field lines that are expected to be coherent at least at latitudes smaller than 65°. This coherence may not be observable at the poles ($|b| > 65°$), where the expansion can open the bubble causing the tangling of field lines. We also expect enhanced magnetic field strength in the cavity walls (see second panel of Fig. 1) due to the squeezing of the field lines into a thin shell. Such a cold, dense, and dusty environment crossed by strong and, in some places, coherent magnetic field lines are fundamental for having dust grain alignment and subsequent polarization (see e.g. Hoang & Lazarian 2009; Hughes et al. 2009).

To study the influence of the bubble over polarization, we produce maps of synthetic Stokes' parameters for three different set-ups: the original simulation (S0), the case in which only the part enclosed by the outer surface of the bubble is considered (S0justLB), and the case where the magnetic field is set only along the $x$ direction (S0uniB) with a strength equal to the mean value of the magnetic field **B** of the simulation. In Table 2, we list an overview of the RT post-processing simulations.

In this section, we discuss in detail the influence that the presence of the cavity has on the column density ($N_H$), on the linear polarized flux ($P_l$), and on the linear polarization fraction ($p_l$) as received by an observer placed inside the bubble. We present the magnetic field lines direction as inferred by the dust polarization angles at 353 GHz and we compare them qualitatively with those observed for the Milky Way by the *Planck* mission. We end the discussion by briefly comparing an open cap with a closed one and pointing out some limits of our work.
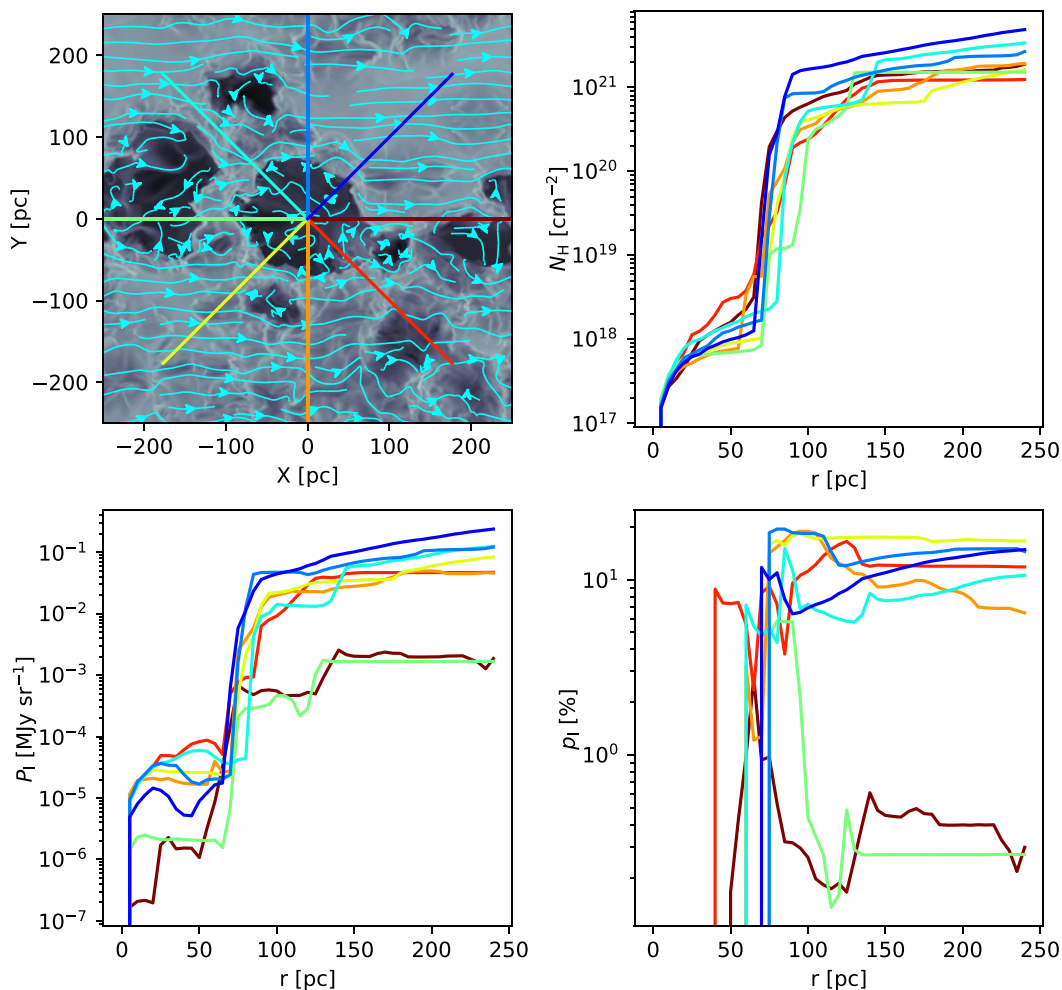
**Figure 6.** Column density ($N_H$), linearly polarized flux ($P_l$), and linear polarization fraction ($p_l$) over distance, as seen by an observer placed at the centre of the cavity, along eight LOSs in the *x*–*y* plane. The eight LOSs chosen are presented in the upper left panel and are the same as Fig. 2.

### 5.1 Cavity and observed polarized emission

In Fig. 5, we present the first derivative of the linearly polarized flux, at 353 GHz, along all the LOSs that lie within the mid-planes as they approach the observer from outside of the simulation domain. From the comparison of these cuts with the corresponding gas density cuts (dust to gas ratio is 1 per cent), in the top panel of Fig. 1, it is clearly visible that the linearly polarized dust emission is correlated to the dust density. Inside the simulated cavities, where the material has been swept away by the energy of SN explosions, there is negligible dust emission; this emission becomes instead important in the densest parts of the simulation, specifically at the cavity walls where magnetic fields are stronger and coherent.

We use the POLARIS ray-tracing simulation to sample the Stokes' parameters and the column density values while the rays are approaching the observer at the centre of the bubble, as described in Section 4.2. In Fig. 6, we report the value of $N_H$, $P_l$, and $p_l$ with respect to the distance from the centre for eight selected LOSs chosen in the *x*–*y* plane and spaced by an angle of 45°. Starting from $r = 0$ pc and moving away from the centre, these three quantities undergo an abrupt change in their values as the inner edge of the cavity is crossed. Moving further through the cavity wall more material is taken into account and this results in a constant increase of $N_H$; instead, the

values of $P_l$ and $p_l$ change more randomly since they depend on the coherence of the magnetic field lines orientation along the LOS as well as the local dust grain alignment efficiency (see e.g. Lazarian & Hoang 2007; Reissl et al. 2020a).

In Fig. 7, we report the normalized two-dimensional histograms for all the LOSs that lie within a given latitude interval [$b \in (-2°, 2°)$; ($-20°, 20°$)]. The 5th, 95th, and 99th percentiles, together with the median, are plotted. The mean distance to the inner surface of the cavity is reported as a vertical line. In these plots, we find a confirmation of the influence of the edges of the bubble on $N_H$, $P_l$, and $p_l$, since these quantities have a consistent variation in their values in correspondence of the cavity borders.

We isolate the contribution from the bubble edges to $N_H$, $I$, $P_l$, and $p_l$ by considering the S0justLB set-up. We report the resulting values for S0 and S0justLB in Table 3. The comparison between the obtained values indicates that the contribution of the edges of the Local Bubble is not negligible with respect to that of the whole simulation.

We know from real observations that the Bubble boundary can be identified as the distance from the observer where the linear polarization fraction in the *V* band reaches a value of ≈0.1 per cent (Gontcharov & Mosenkov 2019). To check if our simulations are in agreement with observations, we use the S0justLB set-up and the
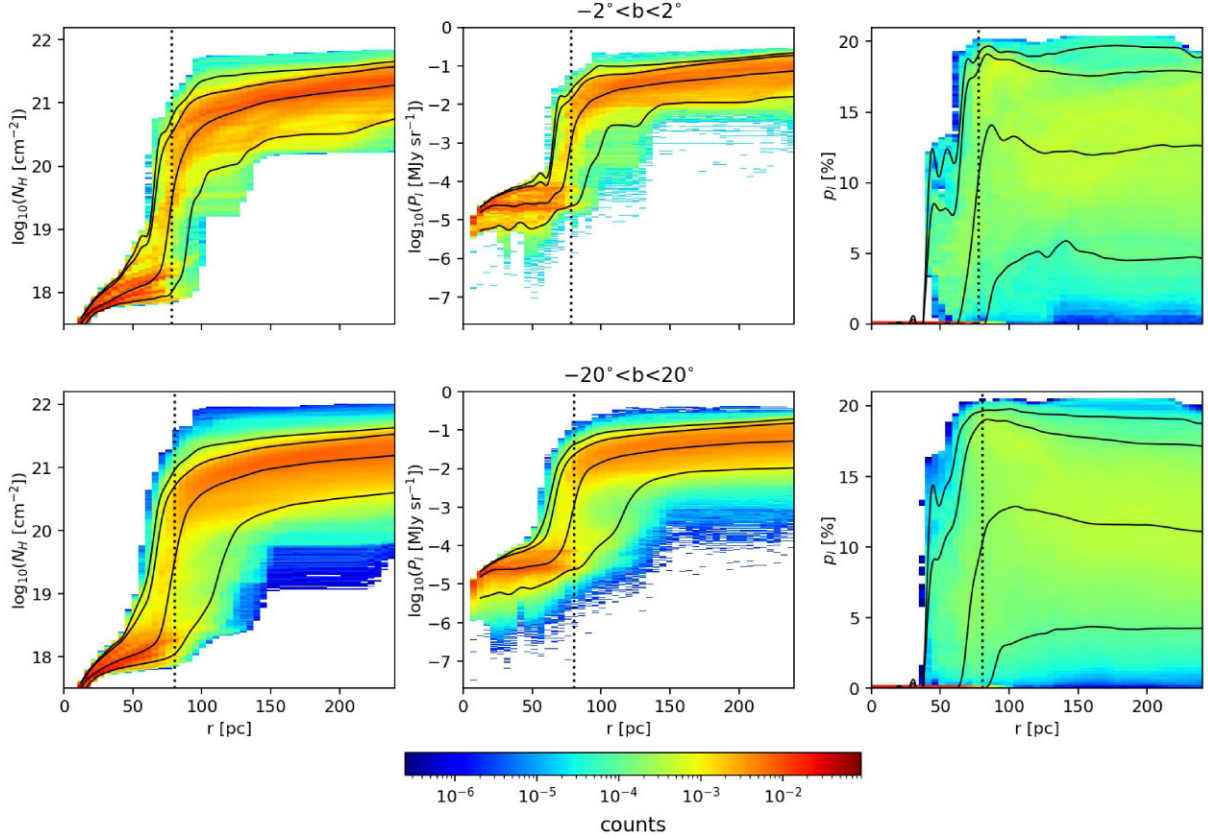
**Figure 7.** Two-dimensional normalized histograms for the column density, the linearly polarized flux, and the linear polarization fraction for all the LOSs that lie within the galactic latitude range indicated in each row. The black solid lines show the 5th, 95th, and 99th percentiles of the data and the median. The black dotted vertical lines indicate the average distance to the inner surface of the Local Bubble candidate.

**Table 3.** Comparison of the column density, intensity, linearly polarized flux, and polarization fraction between S0 and S0justLB. The quantities are computed using all the LOSs and only the LOSs at low and intermediate latitudes ($15° \leq |b| \leq 65°$).

| Quantity | Simulation | Mean | | Median | |
|---|---|---|---|---|---|
| | | All | $15° \leq |b| \leq 65°$ | All | $15° \leq |b| \leq 65°$ |
| $\log_{10}(N_{\mathrm{H}})$ $(\mathrm{cm}^{-2})$ | S0 | 20.97 | 20.76 | 20.72 | 20.60 |
| | S0justLB | 20.34 | 20.21 | 20.12 | 19.97 |
| $I$ $(\mathrm{MJy\,sr}^{-1})$ | S0 | 0.324 | 0.210 | 0.198 | 0.151 |
| | S0justLB | 0.082 | 0.063 | 0.05 | 0.036 |
| $P_{\mathrm{l}}$ $(\mathrm{MJy\,sr}^{-1})$ | S0 | 0.032 | 0.016 | 0.013 | 0.009 |
| | S0justLB | 0.009 | 0.006 | 0.005 | 0.003 |
| $p_{\mathrm{l}}$ (per cent) | S0 | 8.093 | 7.214 | 7.794 | 6.913 |
| | S0justLB | 9.991 | 9.621 | 10.081 | 9.517 |

relation presented in Planck Collaboration (2015),

$$R_{\mathrm{P/p}} = \frac{P_{\mathrm{S}}}{p_{\mathrm{V}}} = [5.4 \pm 0.3]\,\mathrm{MJy\,sr}^{-1}, \tag{4}$$

where $P_{\mathrm{S}}$ is the linear polarized flux at 353 GHz and $p_{\mathrm{V}}$ is the polarization fraction in the visible band. This relation correlates the polarization properties in the sub-millimetre band with the ones in the visible. We obtain a median threshold value for $p_{\mathrm{V}}$ of $\approx 0.12$ per cent, which is comparable with the work of Gontcharov & Mosenkov (2019).
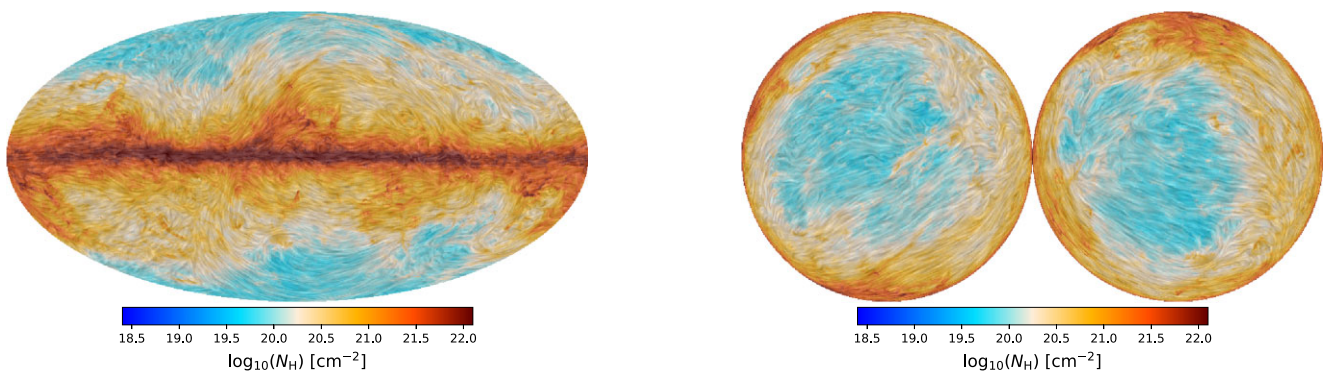
### 5.2 Cavity and polarization angle

We use the Stokes parameters from the RT simulations to compute the polarization angles from the dust emission, which we rotate by $90°$ to obtain the plane-of-the-sky magnetic field orientation. Fig. 8 presents Mollweide and orthographic projections centred at the galactic poles for the column density, $\log_{10}(N_{\mathrm{H}})$, and the inferred magnetic field orientation for the three set-ups described in Table 2. We consider the results into three distinct regions of the sky: the disc mid-plane ($|b| < 15°$), low to intermediate latitudes ($15° \leq |b| \leq 65°$), and the galactic polar regions ($|b| > 65°$).

The Mollweide projection of S0, presented in the top panel of Fig. 8, shows that the magnetic field lines toward the disc mid-
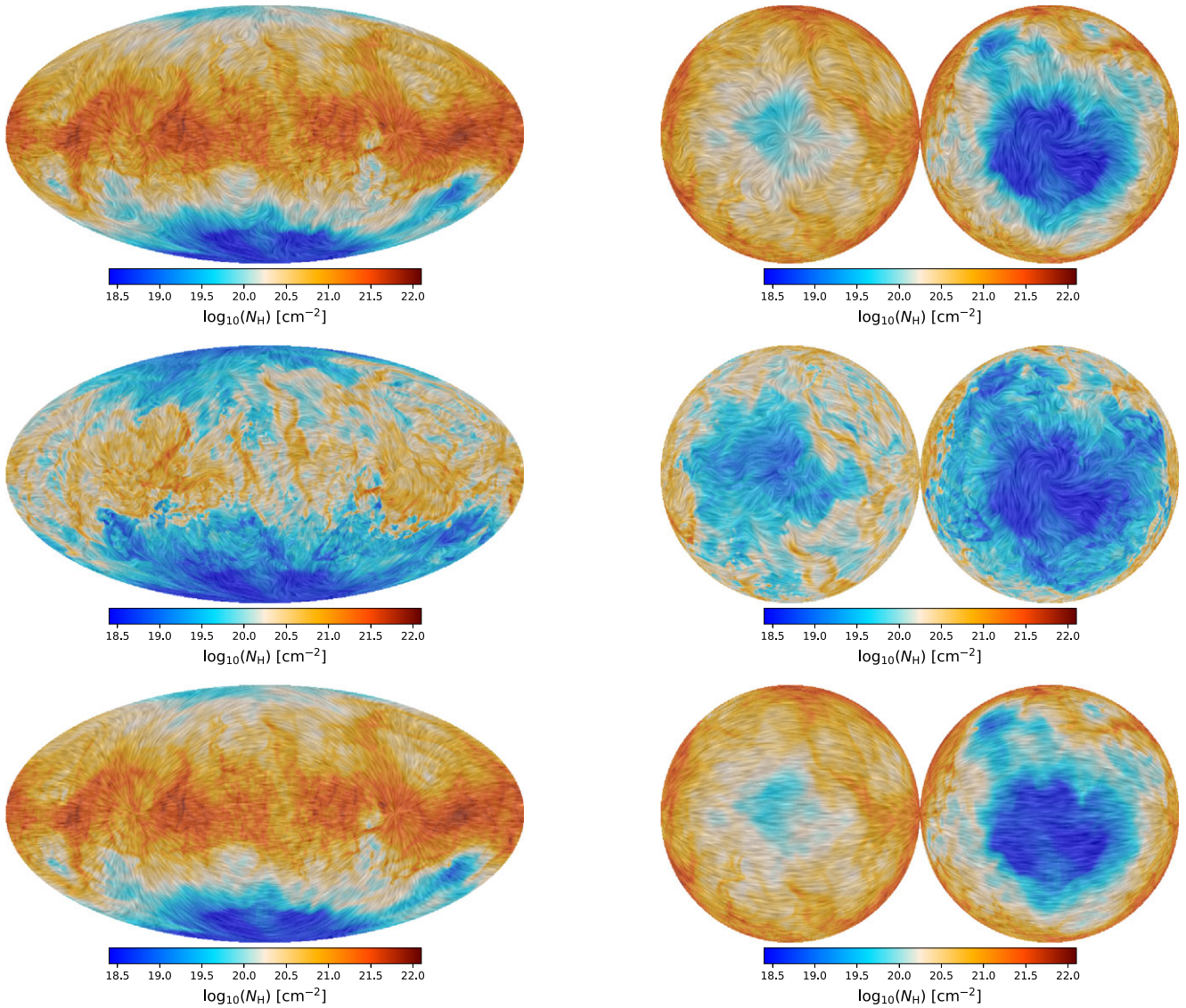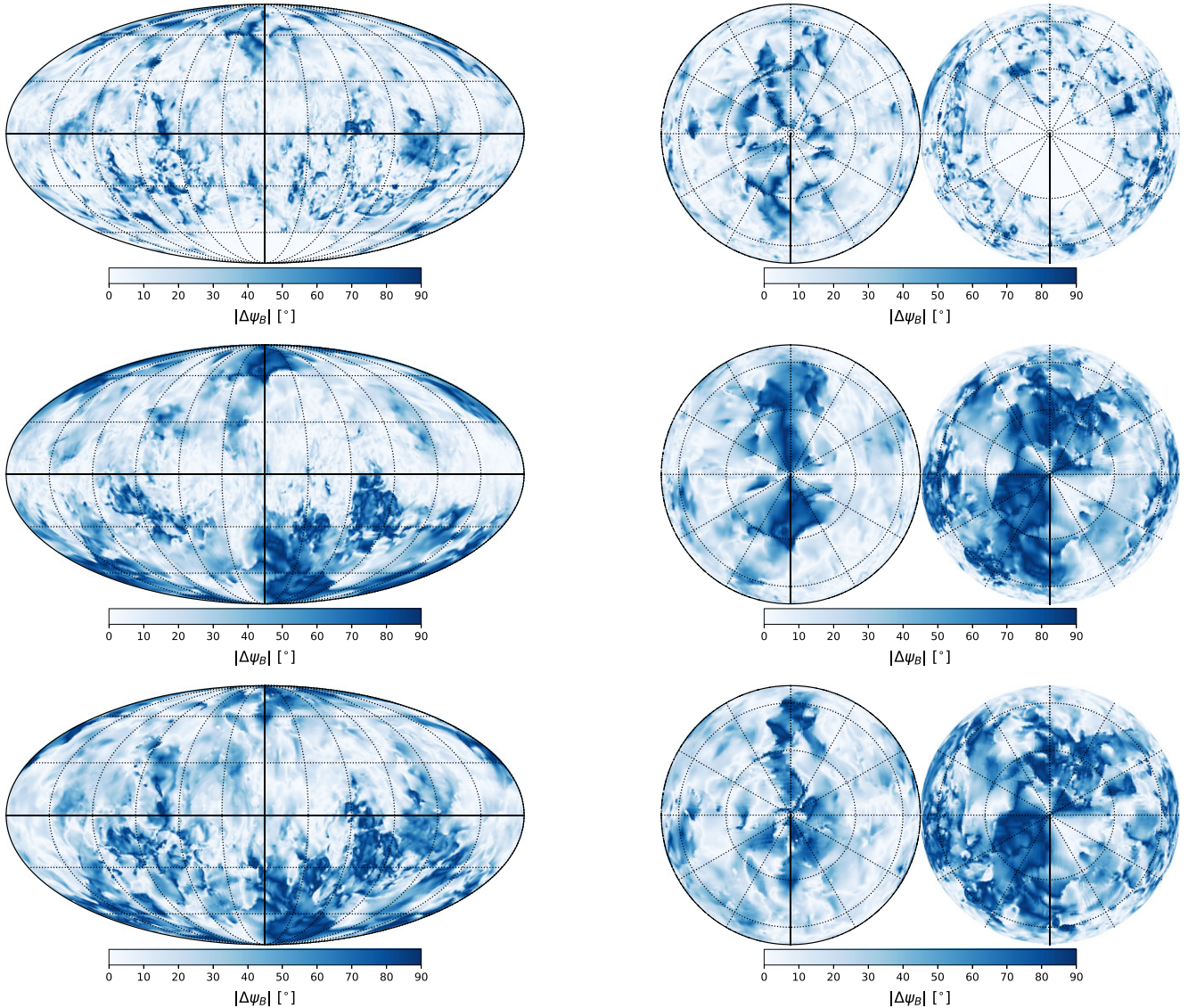
**Figure 8.** Mollweide (*left*) and orthographic projections centred at the galactic poles (*right*) of the column density, $N_H$, and the plane-of-the-sky magnetic field derived from the synthetic 353 GHz polarization, shown by the colours and the drapery pattern, respectively. The drapery pattern is obtained using the line integral convolution (Cabral & Leedom 1993) of the rotated dust polarization vectors. From top to bottom, the panels correspond to the synthetic observations S0, S0justLB, and S0uniB, as introduced in Table 2.



**Figure 9.** The same as Fig. 8 but for actual observational 353 GHz dust emission and polarization data of the *Planck* mission.

**Figure 10.** Mollweide (*left*) and orthographic projections (*right*) of the dust polarization angle difference corresponding to the magnetic field orientation presented in Fig. 8. *Top panel*: difference between the simulations S0 and S0justLB. *Middle panel*: difference between S0 and S0uniB. *Bottom panel*: difference between S0justLB and S0uniB.

plane and at low and intermediate galactic latitudes are relatively homogeneous and parallel to the galactic plane. This homogeneity and orientation are also observed in S0justLB, shown in the middle panel of Fig. 8, where only the volume enclosed by the Local Bubble candidate is considered. In both the set-ups, we find the convergence of the magnetic field lines toward two points in the galactic plane, coinciding with the directions of ( $l$, $b$) $\approx$ ($\pm$90°, 0°).

We interpret the similarity between S0 and S0justLB at low and intermediate galactic latitudes to indicate that the cavity in the simulation inherits the initial mean field orientation from its environment. This is in agreement with theoretical models that assume flux-freezing, i.e. perfect coupling between the matter and the field, to model the magnetic field morphology in the surface of an expanding bubble (see e.g. Ferrière et al. 1991; Alves et al. 2018; Pelgrims et al. 2020). This assumption, added to the general geometry of the expanding shell, results in a relatively homogeneous field parallel to the wall of the cavity and converging towards the poles

set by the initial field orientation. However, at high galactic latitudes, there is a clear discrepancy between our synthetic observations and the homogeneous field lines expected from theoretical models, as we discuss later.

In Fig. 9, we present the equivalent of Fig. 8 but using the data from the *Planck* satellite (Planck Collaboration I 2016a). A comparison between our numerical simulation with observational data at | $b$ | ≲ 15° makes little sense because we are only able to trace the galactic mid-plane within our simulation domain, that is, out to a distance of 250 pc. At low and intermediate galactic latitudes, the comparison is more meaningful, as the dust exponential scale heights in the Milky Way are around 100 and 90 pc for the cold and warm components, respectively, (see e.g. Misiriotis et al. 2006). At these latitudes, we note that our magnetic field lines show a morphological pattern that is qualitatively in agreement with the *Planck* data at 353 GHz. In our synthetic observations, the homogeneous magnetic field results from the initial conditions in the simulation, which is
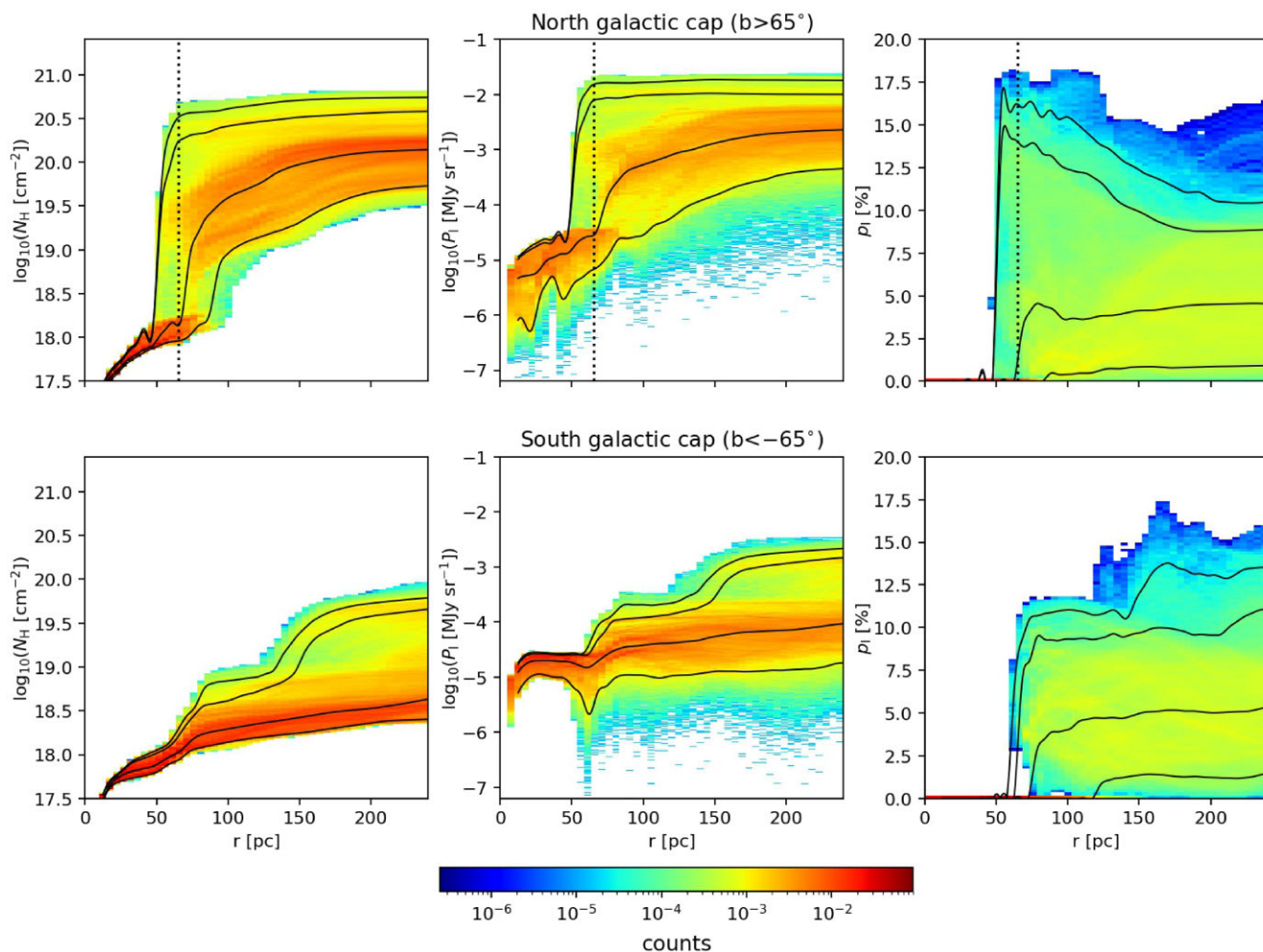
**Figure 11.** Same as Fig. 7, but for the Northern (closed) and Southern (open) galactic caps, defined for the galactic latitudes $b > +65°$ and $b < -65°$, respectively.

an initial magnetic field aligned along the *x* direction. In the case of *Planck* , it is the product of the Galactic magnetic field, which is most likely parallel to the Galactic plane, integrated along the whole LOS, although there are a few regions in the *Planck* map where the observed field orientation seems to be produced by nearby clouds, even at low Galactic latitudes, as, for example, toward the Pipe Nebula (Alves & Franco 2007; Soler et al. 2016). Towards the galactic caps, the reconstructed magnetic field lines exhibit high turbulence and non-homogeneity, contrasting with the *Planck* observations and the previously mentioned theoretical models.

We present the differences in dust polarization angles between the three RT set-ups in Fig. 10, which illustrate the variations of the polarization pattern among these configurations. The angle differences between S0 and S0justLB highlight the deviation in the projected field orientation between the Local Bubble candidate and the background. If the contributions from the cavity to the observed polarization orientation are negligible, we would see large angle differences. If the candidate Local Bubble is the dominant signal determining the observed polarization orientation, we would see negligible angle differences. We find that the angle differences are close to 0° for most of the sky, but there are a considerable number of LOSs for which the difference is up to 90°. This suggests that while the dust and magnetic field in the shell of the Local

Bubble candidate plays a fundamental role in creating the observed polarization patterns, it is not solely responsible for the signal across the whole sky.

The high turbulence of the reconstructed magnetic field lines for our cavity caps is confirmed by the differences in angles between S0 and S0uniB and S0justLB and S0uniB, as shown in the middle and bottom panels of Fig. 10. These significant differences are particularly prominent towards the southern galactic cap, which can be explained by the fact that the simulated Local Bubble is open in that direction. The northern cap also exhibits substantial angle differences, especially in the *y* direction, that is, orthogonal to the initial mean field orientation. Most likely, the non-regularity and non-homogeneity of the polarization angle towards the poles are caused by the bubble expansion, which is responsible for the ejection of material from the disc and the possible break-up of the cavity towards the poles, with the consequence that the magnetic field lines become tangled.

Our results indicate that variations in the field direction introduced by either turbulence in the shell or the fragmentation of its walls are significant in explaining the morphological pattern obtained for our Local Bubble candidate. These effects are typically not included in the flux-freezing theoretical models (see e.g. Ferriere et al. 1991). However, our MHD simulations do not incorporate a global toroidal magnetic field component, which is typically present in rotationally

supported spiral galaxies (Beck 2013; Borlaff et al. 2021). This leads to a dichotomy: either the Local Bubble is singularly homogeneous in comparison to the bubble produced in our simulations, or the homogeneous field orientation observed towards the poles in the *Planck* polarization data is a result of the combined effects of the dust and magnetic field present behind the Local Bubble.

Further investigation is required to determine whether the plane-of-the-sky field homogeneity at high Galactic latitudes can be attributed to the field in the Local Bubble shell or a coherent large-scale field component is necessary. Resolving these issues requires the analysis of numerical simulations that produce realistic Local Bubble analogues embedded in a highly resolved full disc galaxy. These are not available yet.

### 5.3 Open versus closed cap

SN explosions generate expanding bubbles that can break out of the galactic disc and subsequently expand into the halo. This is one of the known processes that can cause the galactic fountain flows (see e.g. Bregman 1980; Bish et al. 2019; Grand et al. 2019). Observational evidence suggests that the Local Bubble shell has been blown out of the disc above and below the Galactic plane, and could be a galactic chimney (Welsh et al. 1999). Our Local Bubble candidate has an open and a closed cap, which will break in turn in about 10 Myr, as observed from the analysis of the subsequent snapshots. We would like to know if it is possible to distinguish between the two configurations through polarization observations.

In Fig. 11, we report the relative normalized 2D-Histograms regarding $N_H$, $P_l$, and $p_l$. As expected, the open cap presents low column density and low polarized flux values compared to the closed one. This is due to the fact that in the south direction, the gas has been swept from the simulation domain, and the radiation encounters, during its path towards the observer, just some rarefied and isolated clouds of gas that are still inside the bubble; see for example, the top panel of Fig. 1. Furthermore, $N_H$ and $P_l$ in the case of an open cap do not undergo a sharp change in their values as in the case of a closed one.

From the orthographic projection in the top panel of Fig. 8, the magnetic field morphology towards the caps can be appreciated. We note that it would be difficult to determine which one is the open and the closed cap, just from the field morphology alone.

### 5.4 Caveats

To produce our synthetic observations, we choose a simulation that follows the dynamical evolution of the complex multiphase ISM in a $500 \times 500 \times 500 \, pc^3$ volume. The physical properties of the environment, such as the gas density, gas temperature, and magnetic field in our simulation are comparable to the ones of the solar neighbourhood, although cosmic rays are missing. The resolution of our simulation (512 cells per side) allows us to resolve the structure of the ISM in the walls of the Local Bubble candidate, but it limits our study to a portion of the ISM and not to an entire galaxy.

To study the influence of the bubble on the polarization data received by an observer inside it, we isolate the shell of the cavity. However, we acknowledge that our method may not accurately identify the bubble walls in certain directions due to the complexity of gas distribution. Nevertheless, we evaluate the robustness of our results by making slight manual adjustments to the thickness of the bubble walls. We confirm that these modifications do not significantly affect our results.

In our simulation, we have SN explosions which are responsible for blowing cavities that structure the ISM similarly to ours and for

ejecting material from the disc, although it is possible that we are underestimating the amount of ejected gas and dust, or that the ejected material is lost from the simulation domain. The ideal numerical set-up for this study should include the large-scale field resulting from the Galactic dynamics and the numerical resolution to detail the structure of the Local Bubble candidates. However, such a numerical experiment is challenging for the current computational facilities.

### 6 CONCLUSIONS

We performed an analysis of synthetic dust polarization observations for an observer in the centre of a simulated SN-blown cavity with properties similar to the Local Bubble around the Sun. We found that the Local Bubble walls make a non-negligible contribution to the polarized radiation at 353 GHz detected inside the cavity. This stresses the importance of studying the Local Bubble in detail since all electromagnetic information from objects beyond the cavity must be observed through this local veil of material.

Specifically, we compared our synthetic dust polarization maps with data from the *Planck* satellite (Planck Collaboration I 2016a). For this, we distinguished three distinct regions on the sky: the disc mid-plane ($|b| < 15°$), low to intermediate latitudes ($15° \leq |b| \leq 65°$), and the galactic polar regions ($|b| > 65°$).

Because the numerical simulation we used to extract the cavity only allows us to trace the galactic mid-plane out to a distance of 250 pc (Girichidis et al. 2018; Girichidis 2021), comparing to observational data at $|b| \lesssim 15°$ makes little sense since the full disc is missing. The analysis of this region on the sky will need to be the topic of future studies in which Local Bubble analogues are extracted from high-resolution simulations of the full Galactic disc with star formation, stellar feedback, and a realistic multiphase description of the ISM. However, we note that already our current model is able to reproduce the observed convergence points of the field at $l \approx \pm 90°$.

At low and intermediate galactic latitudes ($15° \leq |b| \leq 65°$), we found that the magnetic field lines, inferred from dust synthetic polarization observations, display an overall morphological pattern and polarization degree in good agreement with current models of the magnetic field structure in the Local Bubble walls (see e.g. Alves et al. 2018) and with the *Planck* data at 353 GHz (Planck Collaboration I 2016a).

Observations of the polarization around the North and South Galactic Poles ($|b| > 65°$) indicate a highly regular and coherent magnetic field structure (Planck Collaboration XLIV 2016c). Our simulations are in tension with these results, as we found a high degree of small-scale structures, caused by the local turbulence in the expanding bubble walls, as well as indications of open field lines, consistent with the fact that one of the caps of the studied cavity has already burst open into the low-density gas above the disc mid-plane, and the other cap is expected to do so in a few Myr. As our local ISM model has no global toroidal magnetic field component, as is characteristic for rotationally supported spiral galaxies (Beck 2013; Borlaff et al. 2021), we conclude that a coherent large-scale field component may be necessary for explaining the observed polarization pattern at high Galactic latitudes. Again, this emphasizes the need for conducting high-resolution global disc simulations to investigate this further. An alternative explanation could be that our Local Bubble candidate has an unrealistically high level of turbulence and fragmentation. It is therefore important to further study the gas dynamical properties of the Local Bubble and better measure the local velocity dispersion as function of distance from the Sun in different directions.

Finally, we note that given the current estimates of structure and spatial extent of the Local Bubble (e.g. Alves et al. 2018; Pelgrims et al. 2020; Zucker et al. 2022), it seems likely that the cavity is in the process of bursting into the low-density gas above the disc mid-plane, or has already done so. Our results indicate that it is difficult to distinguish between an open and a closed galactic cap based only on the field morphology derived from polarization measurements. Further data are required, ideally, from the combination of dust extinction measurements and starlight polarization observations to obtain an estimate of the three-dimensional magnetic field structure of our nearby Galactic environment.

## DATA AVAILABILITY

The Local Bubble candidate simulation data are publicly available at http://silcc.mpa-garching.mpg.de. The RT code POLARIS is available at https://portia.astrophysik.uni-kiel.de/polaris/. The synthetic observations maps and the analysis scripts will be shared upon request.

## REFERENCES

Alves F. O., Franco G. A. P., 2007, A&A, 470, 597
Alves M. I. R., Boulanger F., Ferrière K., Montier L., 2018, A&A, 611, L5
Andersson B. G., Lazarian A., Vaillancourt J. E., 2015, ARA&A, 53, 501
Beck R., 2013, in Beck R., Balogh A., Bykov A., Treumann R. A., Widrow L., eds, Space Sci. Ser. ISSI Vol. 39, Large-Scale Magnetic Fields in the Universe. Springer, New York, p. 215
Bialy S. et al., 2021, ApJ, 919, L5
Bish H. V., Werk J. K., Prochaska J. X., Rubin K. H. R., Zheng Y., O'Meara J. M., Deason A. J., 2019, ApJ, 882, 76
Bjorkman J. E., Wood K., 2001, ApJ, 554, 615
Borlaff A. S. et al., 2021, ApJ, 921, 128
Bracco A., Bresnahan D., Palmeirim P., Arzoumanian D., André P., Ward-Thompson D., Marchal A., 2020, A&A, 644, A5
Bregman J. N., 1980, ApJ, 236, 577
Breitschwerdt D., Feige J., Schulreich M. M., Avillez M. A. D., Dettbarn C., Fuchs B., 2016, Nature, 532, 73
Cabral B., Leedom L. C., 1993, in Special Interest Group on GRAPHics and Interactive Techniques Proceedings. Lawrence Livermore National Lab., CA, p. 263, available at: https://www.osti.gov/biblio/10185520
Camps P. et al., 2015, A&A, 580, A87
Chabrier G., 2003, PASP, 115, 763
Cox D. P., Reynolds R. J., 1987, ARA&A, 25, 303
Cox D. P., Smith B. W., 1974, ApJ, 189, L105
Dohnanyi J. S., 1969, J. Geophys. Res., 74, 2531
Draine B. T., 1996, in Roberge W. G., Whittet D. C. B., eds, ASP Conf. Ser. Vol. 97, Polarimetry of the Interstellar Medium. Astron. Soc. Pac., San Francisco, p. 16
Ferrière K. M., Mac Low M.-M., Zweibel E. G., 1991, ApJ, 375, 239
Fuchs B., Breitschwerdt D., De Avillez M. A., Dettbarn C., Flynn C., 2006, MNRAS, 373, 993
Galeazzi M. et al., 2014, Nature, 512, 171
Girichidis P., 2021, MNRAS, 507, 5641
Girichidis P. et al., 2016, MNRAS, 456, 3432
Girichidis P., Seifried D., Naab T., Peters T., Walch S., Wünsch R., Glover S. C. O., Klessen R. S., 2018, MNRAS, 480, 3511
Gontcharov G. A., Mosenkov A. V., 2019, MNRAS, 483, 299
Górski K. M., Hivon E., Banday A. J., Wandelt B. D., Hansen F. K., Reinecke M., Bartelmann M., 2005, ApJ, 622, 759
Grand R. J. J. et al., 2019, MNRAS, 490, 4786
Gry C., Jenkins E. B., 2017, A&A, 598, A31
Heiles C., 1996, ApJ, 462, 316
Heiles C., 2000, AJ, 119, 923
Herranen J., Lazarian A., Hoang T., 2019, ApJ, 878, 96
Hoang T., Lazarian A., 2009, ApJ, 697, 1316
Hoang T., Lazarian A., 2013, MNRAS, 438, 680
Hoang T., Lazarian A., Martin P. G., 2014, ApJ, 790, 6
Hughes A. M., Wilner D. J., Cho J., Marrone D. P., Lazarian A., Andrews S. M., Rao R., 2009, ApJ, 704, 1204
Hunt C. P., Moskowitz B. M., Banerjee S. K., 1995, Magnetic Properties of Rocks and Minerals. American Geophysical Union (AGU), Washington DC, p. 189
Jones T. W., Hardee P. E., 1979, ApJ, 228, 268
Kennicutt R. C., Jr, 1998, ApJ, 498, 541
Krause M. G. H., Hardcastle M. J., 2021, MNRAS, 502, 2807
Krause M., Fierlinger K., Diehl R., Burkert A., Voss R., Ziegler U., 2013a, A&A, 550, A49
Krause M., Charbonnel C., Decressin T., Meynet G., Prantzos N., 2013b, A&A, 552, A121
Lallement R., Welsh B. Y., Vergely J. L., Crifo F., Sfeir D., 2003, A&A, 411, 447
Lallement R., Vergely J. L., Valette B., Puspitarini L., Eyer L., Casagrande L., 2014, A&A, 561, A91
Lazarian A., Hoang T., 2007, MNRAS, 378, 910
Linsky J. L., Redfield S., 2021, ApJ, 920, 75
Linsky J. L., Redfield S., Tilipman D., 2019, ApJ, 886, 41
Lucke P. B., 1978, A&A, 64, 367
Lucy L. B., 1999, A&A, 344, 282
Martin P. G., 1971, MNRAS, 153, 279
Mathis J. S., Rumpl W., Nordsieck K. H., 1977, ApJ, 217, 425
Mathis J. S., Mezger P. G., Panagia N., 1983, A&A, 128, 212
Misiriotis A., Xilouris E. M., Papamastorakis J., Boumis P., Goudis C. D., 2006, A&A, 459, 113
Ober F., Wolf S., Uribe A. L., Klahr H. H., 2015, A&A, 579, A105
Pelgrims V., Ferrière K., Boulanger F., Lallement R., Montier L., 2020, A&A, 636, A17
Planck Collaboration XXI, 2015, A&A, 576, A106
Planck Collaboration I, 2016a, A&A, 594, A1

Planck Collaboration XLII, 2016b, A&A, 596, A103
Planck Collaboration XLIV, 2016c, A&A, 596, A105
Planck Collaboration IX, 2020, A&A, 641, A11
Puspitarini L., Lallement R., Vergely J. L., Snowden S. L., 2014, A&A, 566, A13
Reissl S., Wolf S., Brauer R., 2016, A&A, 593, A87
Reissl S., Brauer R., Klessen R. S., Pellegrini E. W., 2019, ApJ, 885, 15
Reissl S., Guillet V., Brauer R., Levrier F., Boulanger F., Klessen R. S., 2020a, A&A, 640, A118
Reissl S. et al., 2020b, A&A, 642, A201
Sanders W. T., Kraushaar W. L., Nousek J. A., Fried P. M., 1977, ApJ, 217, L87
Schmidt M., 1959, ApJ, 129, 243
Schulreich M., Breitschwerdt D., Feige J., Dettbarn C., 2018, Galaxies, 6, 26
Snowden S. L. et al., 1997, ApJ, 485, 125
Snowden S. L. et al., 2014, ApJ, 791, L14
Snowden S. L., Heiles C., Koutroumpa D., Kuntz K. D., Lallement R., McCammon D., Peek J. E. G., 2015, ApJ, 806, 119
Soler J. D. et al., 2016, A&A, 596, A93
Soler J. D., Bracco A., Pon A., 2018, A&A, 609, L3
Sun X. H., Reich W., Waelkens A., Enßlin T. A., 2008, A&A, 477, 573
Walch S. et al., 2015, MNRAS, 454, 238
Welsh B. Y., Sfeir D. M., Sirk M. M., Lallement R., 1999, A&A, 352, 308
Xu J., Han J. L., 2019, MNRAS, 486, 4275
Zucker C. et al., 2022, Nature, 601, 334

## APPENDIX A: SIMULATING A LOCAL BUBBLE

### A1 Details of the numerical set-up

We use the numerical simulations from Girichidis et al. (2018) and Girichidis (2021), which are part of the SILCC project (Walch et al.

2015; Girichidis et al. 2016). The setup covers a domain of $500 \times 500 \times 500\,\mathrm{pc}^3$ in size. Initially, the gas is uniformly distributed in the $xy$ plane with a vertical stratification in $z$. The gas is initially at rest. We analyse two simulations, hereafter referred to as B3-1pc and B6-1pc, with an initial magnetic field set along the $x$ direction and with a central intensity of $B(z = 0) = 3\,\mu\mathrm{G}$ and $B(z = 0) = 6\,\mu\mathrm{G}$, respectively. The magnetic field strength scales in the vertical direction as $B(z) = B(z = 0)(\rho(z)/\rho(z = 0))^{1/2}$. The three-phase medium including the filaments, clouds, and voids is the result of SN driving. The SN explosions rate is constant and based on the Kennicutt–Schmidt (KS) relation (Schmidt 1959; Kennicutt 1998) for star formation. Assuming the initial mass function presented in Chabrier (2003), the star formation rate surface density from the KS relation translates into an SN rate of $15\,\mathrm{Myr}^{-1}$ for the simulation box, where every star above eight solar masses explodes as an SN.

The SN explosions in the selected simulation set are a mixture of 20 per cent Type Ia and 80 per cent Type II. The Type Ia SN explosions have a uniform distribution in $x$ and $y$ and a normal distribution in $z$ with a scale height of 300 pc. The Type II SN explosions are split between individual SN explosions and clustered ones. The individual SN explosions, which correspond to 60 per cent of the Type II, are placed randomly in the $x$–$y$ plane and normally distributed in $z$ with a scale height of 50 pc. The remaining 40 per cent of the Type II are clustered assuming clusters with a lifetime of 40 Myr and a total number of SN explosions, $N$, ranging between 7 and 20, randomly drawn from a distribution with a probability scaling with $N^{-2}$.

The time evolution of the gas distribution is shown in Fig. A1 for B3-1pc (top panels) and B6-1pc (bottom panels) with some identified bubbles marked with blue crosses. The most prominent and largest bubbles correspond to clustered SN feedback.
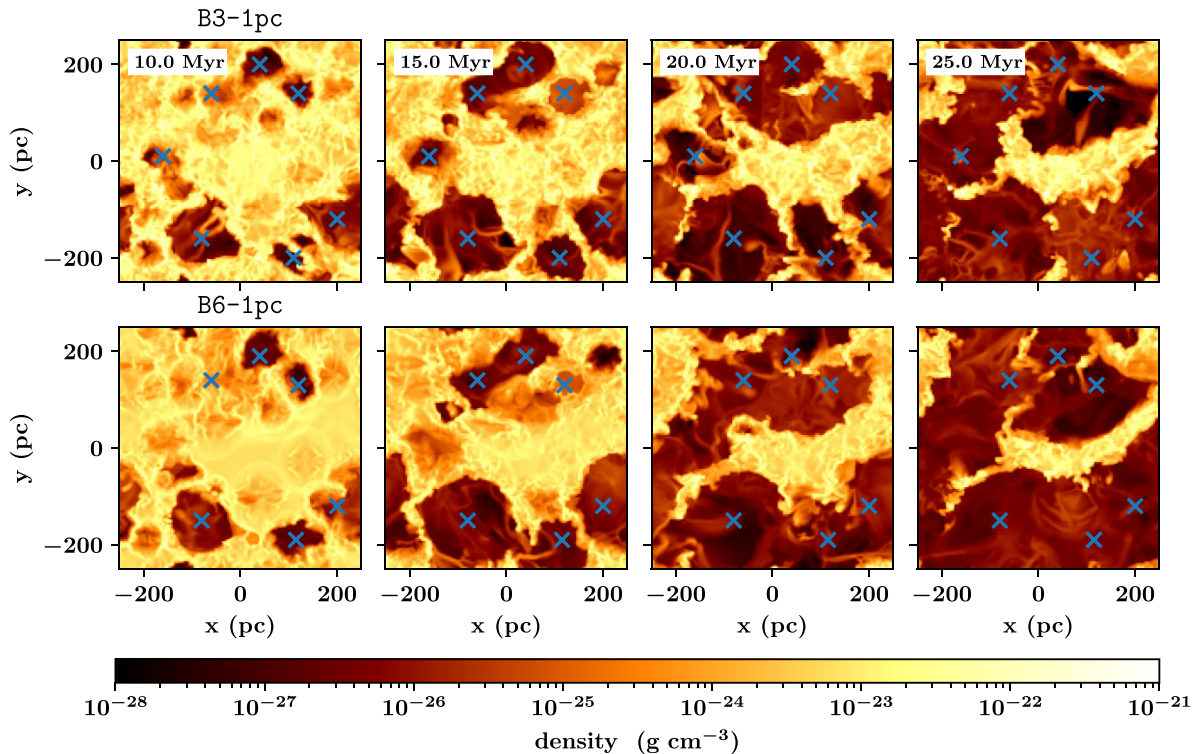
**Figure A1.** Density at the mid-plane for two different simulations, B3-1pc (top) and B6-1pc (bottom) for different simulation times (from left to right). The initial candidate positions for the bubble search are shown in blue crosses. Only at early times, we satisfy the constraints for the number of SNe that drives the bubble (∼15).
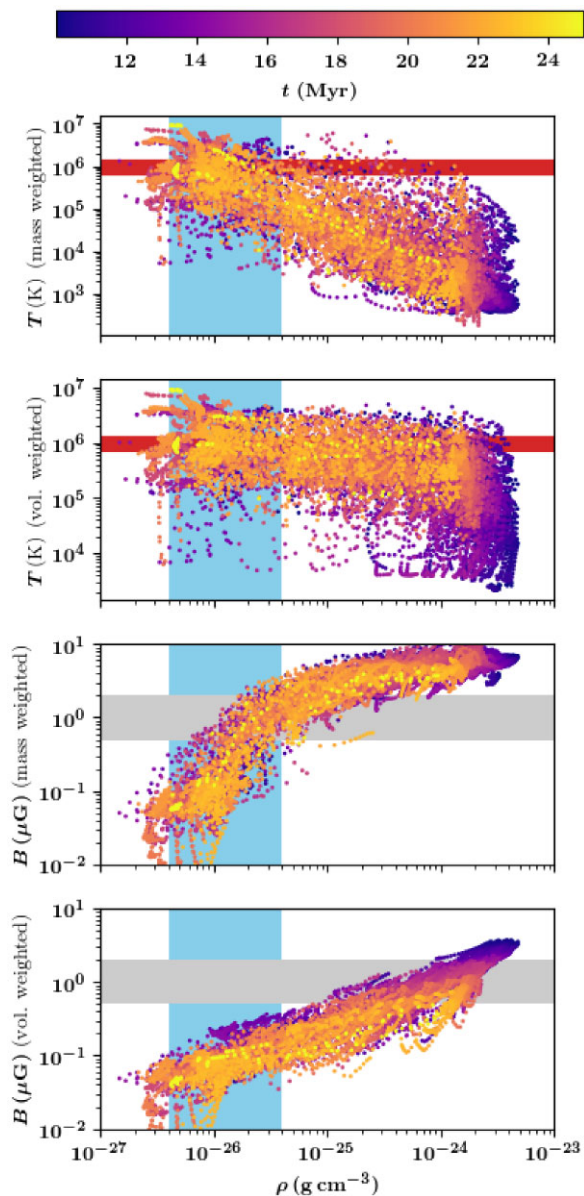
**Figure A2.** All bubbles from the B3-1pc simulation. Every tenth snapshot from 10 to 39 Myr is included. Shaded areas are approximate observational constraints. Colour-coded is the simulation time. In the early stages, the clouds are denser and colder (dark blue points) compared to later times. If we consider the volume-weighted magnetic field, no bubble falls into the desired range of observational values. However, we only miss the range by less than a factor of 1.5. The mass-weighted counterparts fit very well.

## A2 Identification of the Local Bubble in the simulations

Initially, we select a set of cavities by eye in each simulation and identified their central position $\boldsymbol{p}_0 = [x_0, y_0, z_0]$. For each candidate, we investigate spheres around $\boldsymbol{p}_0$ with radius $r$ between 40 and 70 pc. We compute the average density, the total mass in ionized gas, and the mass- and volume-weighted magnetic field and temperature.

Among all the spheres for each candidate, we select the ones which satisfy the following conditions:

(i) $10^{-27}\,\mathrm{g\,cm^{-3}} \leq \rho \leq 4 \times 10^{-26}\,\mathrm{g\,cm^{-3}}$;

(ii) $T \geq 5 \times 10^5\,\mathrm{K}$;

(iii) $0.5\,\mu\mathrm{G} \leq B \leq 2\,\mu\mathrm{G}$.

For the magnetic field strength, we use a selection criterion which corresponds nicely to the values measured by Xu & Han (2019). The magnetic field volume-weighted quantities are below 1 μG. The mass-weighted field directly reflects the field in the shell of the bubble, since the shell mass dominates over the mass in the void. In B3-1pc, the mass-weighted field of the bubble as a function of radius quickly exceeds the value of 2 μG (upper limit in Xu & Han 2019), as a result of local compression with respect to the initial field value. For this reason, we decided to use the B3-1pc instead of the B6-1pc simulation.

A scatter plot with the selected bubbles is depicted in Fig. A2 showing from top to bottom the mass and volume-weighted temperature as well as magnetic field strength as a function of average cloud radius. The observational constraints are depicted in shaded colour. The colour coding of the points corresponds to the simulation time.

## APPENDIX B: DUST HEATING, GRAIN ALIGNMENT, AND SYNTHETIC POLARIZATION MAPS WITH POLARIS

POLARIS is a three-dimensional Monte Carlo (MC) dust continuum RT code dedicated to post-process MHD simulations (Reissl et al. 2016). The code, making use of the physical quantities (e.g. density, temperature, velocity, and magnetic fields) provided by MHD simulations together with an arbitrary number of radiation sources, can compute among other things the dust temperature, the grain alignment efficiency, and produce synthetic multiwavelength intensity and polarization maps.

Linear and circular polarization arise from non-spherical dust grains; these elongated grains have the tendency to align their minor axis with the magnetic field direction and to emit light preferentially along their major. It is therefore necessary to define a specific dust model beforehand e.g. resembling the conditions in the ISM (see Section 4.1). The corresponding cross-sections, for sub-mm emission, can be computed as

$$C_{\mathrm{x}} = \int_{a_{\mathrm{min}}}^{a_{\mathrm{max}}} N_{\mathrm{d}}(a) \big[ C_{\perp}(a) + C_{\parallel}(a) \big] \, \mathrm{d}a, \tag{B1}$$

and

$$\Delta C_{\mathrm{x}} \cong \sin^2 \theta \int_{a_{\mathrm{alg}}}^{a_{\mathrm{max}}} R(a) N_{\mathrm{d}}(a) \times \big[ C_{\perp}(a) - C_{\parallel}(a) \big] \, \mathrm{d}a. \tag{B2}$$

Here, the quantity $C_X$ may represent the cross-sections of extinction, scattering, and absorption whereas $a_{\mathrm{alg}}$ is the minimal radius of grain alignment, $\theta$ is the angle between the magnetic field direction, and the LOS, $R(a)$ is the Rayleigh reduction factor accounting for the grain alignment efficiency, $C_{\perp}(a)$ and $C_{\parallel}(a)$, respectively, are the pre-calculated cross-sections perpendicular and parallel to the grain minor principal axis (see Reissl et al. 2016). POLARIS calculates then the radiation field based on an MC approach in multiple wavelengths $\lambda$. Once the radiation field is defined, the dust temperature $T_{\mathrm{d}}$ is determined assuming an equilibrium between the absorption of photons, and thermal dust emission (Lucy 1999; Bjorkman & Wood 2001; Reissl et al. 2016) as well as the grain alignment efficiency.

For the computation of the grain alignment efficiency, a key aspect in modelling synthetic dust polarization, POLARIS follows the physics of the radiative torque alignment theory (RAT; Lazarian & Hoang 2007). The hallmark of this theory is that anisotropic radiation spins-up irregular grains which subsequently align, in the case of

paramagnetic grains, with the magnetic field direction; this effect is opposed by the random gas particles bombardment. The spin-up process can be quantified by the ratio (Lazarian & Hoang 2007; Hoang & Lazarian 2013)

$$\left(\frac{J_{\mathrm{RAT}}}{J_{\mathrm{g}}}\right)^2 \propto a \left(\frac{1}{n_{\mathrm{g}}} T_{\mathrm{g}} \int \lambda Q_{\mathrm{RAT}} \gamma_\lambda u_\lambda \mathrm{d}\lambda\right)^2, \qquad (\mathrm{B3})$$

where $J_{\mathrm{RAT}}$ and $J_{\mathrm{g}}$ are the dust grain angular momentum induced, respectively, by radiation and by gas collisions. Based on the properties of the MC calculated radiation field POLARIS determines the anisotropy factor $\gamma_\lambda$ and the energy density $u_\lambda$ (for a detailed description, we refer to Reissl et al. 2020a). For the grain alignment efficiency, $Q_{\mathrm{RAT}}$, the following parametrization is used

$$Q_{\mathrm{RAT}} = \cos\Psi \begin{cases} 0.4 & \text{if } \lambda \leq 1.8\,a, \\ 0.4 \times \left(\frac{\lambda}{1.8\,a}\right)^{-2.6} & \text{otherwise,} \end{cases} \qquad (\mathrm{B4})$$

which is based on the average of a large ensemble of different grain shapes (Herranen, Lazarian & Hoang 2019). In equation (B4), $\Psi$ is the angle between the anisotropic radiation field and the magnetic field direction (for details, see Lazarian & Hoang 2007; Reissl et al. 2016, 2020a).

Dust grains with a stable alignment are the ones with the ratio $J_{\mathrm{RAT}}/J_{\mathrm{g}} > 3$ (see e.g. Hoang & Lazarian 2013, for details); it is then possible to compute a characteristic grain size $a_{\mathrm{alg}}$, defined as the size where $J_{\mathrm{RAT}}/J_{\mathrm{g}} = 3$, above which all paramagnetic grains ($a > a_{\mathrm{alg}}$) i.e. will contribute to the dust polarization $R(a) = 1$. Otherwise, for grain sizes $a < a_{\mathrm{alg}}$ the Rayleigh reduction factor is $R(a) = 0$. Furthermore, POLARIS allows only silicate grains to align but graphite grains cannot due to their different paramagnetic properties (see e.g. Hunt, Moskowitz & Banerjee 1995; Draine 1996; Hoang, Lazarian & Martin 2014; Andersson et al. 2015). Hence, $R(a) = 0$ for all considered graphite grain sizes.

Once the dust temperature and the grain alignment efficiency are computed, POLARIS can be used to simulate synthetic multi-wavelength intensity and polarization maps. To accomplish this, the code solves the RT equation in all four Stokes parameters **S** simultaneously. This problem, in the most general form, can be expressed as (see e.g. Martin 1971; Jones & Hardee 1979)

$$\frac{\mathrm{d}}{\mathrm{d}\ell}\mathbf{S} = -\hat{K}\mathbf{S} + \mathbf{J}, \qquad (\mathrm{B5})$$

where **J** the emissivity and $\hat{K}$ the $4 \times 4$ Müller's matrix describing the extinction, absorption, and emission are fully defined by the cross-sections defined in equation (B1) and equation (B2), respectively. Consequently, the emitted total and linearly polarized intensity $I$ and $P_{\mathrm{l}}$, respectively, along each LOS accumulate as

$$\mathrm{d}I \propto n_{\mathrm{g}} C_{\mathrm{abs}} B_\lambda(T_{\mathrm{d}})\mathrm{d}\ell, \qquad (\mathrm{B6})$$

and

$$\mathrm{d}\ell P_{\mathrm{l}} \propto n_{\mathrm{g}} \Delta C_{\mathrm{abs}} \times B_\lambda(T_{\mathrm{d}})\mathrm{d}\ell, \qquad (\mathrm{B7})$$

where $n_{\mathrm{g}}$ is the gas number density, $B_\lambda(T_{\mathrm{d}})$ is the Planck function.

POLARIS solves equation (B5) along the LOS for each path element $\mathrm{d}\ell$ by utilizing a Runge–Kutta solver (see e.g. Ober et al. 2015; Reissl et al. 2019). Moreover, the code allows the definition of plane detectors, for an observer placed outside the grid, or of HEALPIX detectors for an observer placed inside the simulation. For more technical details about POLARIS, we again refer the reader to Reissl et al. (2016, 2019, 2020a), respectively.

This paper has been typeset from a TEX/LATEX file prepared by the author.